Remote z-scanning with a macroscopic voice coil motor for fast 3D multiphoton laser scanning microscopy

Peter Rupprecht,[1,2] Andrew Prendergast,[3,4,5,6] Claire Wyart,[3,4,5,6] and Rainer W Friedrich[1,2,*]

[1]Friedrich Miescher Institute for Biomedical Research, Maulbeerstrasse 66, 4058 Basel, Switzerland
[2]University of Basel, 4003 Basel, Switzerland
[3]Institut du Cerveau et de la Moelle Épinière (ICM), 75013 Paris, France
[4]Inserm UMRS 1127, France
[5]CNRS UMR 7225, France
[6]UPMC Univ Paris 06, F75005, Paris, France
[*]Rainer.Friedrich@fmi.ch

Abstract: There is a high demand for 3D multiphoton imaging in neuroscience and other fields but scanning in axial direction presents technical challenges. We developed a focusing technique based on a remote movable mirror that is conjugate to the specimen plane and translated by a voice coil motor. We constructed cost-effective z-scanning modules from off-the-shelf components that can be mounted onto standard multiphoton laser scanning microscopes to extend scan patterns from 2D to 3D. Systems were designed for large objectives and provide high resolution, high speed and a large z-scan range (>300 μm). We used these systems for 3D multiphoton calcium imaging in the adult zebrafish brain and measured odor-evoked activity patterns across >1500 neurons with single-neuron resolution and high signal-to-noise ratio.

OCIS codes: (180.6900) Three-dimensional microscopy; (120.5800) Scanners; (120.4880) Optomechanics; (170.0170) Medical optics and biotechnology; (170.5810) Scanning microscopy; (170.5380) Physiology.

References and links

1. W. Denk, J. H. Strickler, and W. W. Webb, "Two-photon laser scanning fluorescence microscopy," Science **248**(4951), 73–76 (1990).
2. B. F. Grewe, F. Helmchen, and B. M. Kampa, "Two-photon imaging of neuronal network dynamics in neocortex," in *Optical Imaging of Neocortical Dynamics* (Springer, 2014), pp. 133–150.
3. C. Stosiek, O. Garaschuk, K. Holthoff, and A. Konnerth, "In vivo two-photon calcium imaging of neuronal networks," Proc. Natl. Acad. Sci. U.S.A. **100**(12), 7319–7324 (2003).
4. K. Svoboda and R. Yasuda, "Principles of two-photon excitation microscopy and its applications to neuroscience," Neuron **50**(6), 823–839 (2006).
5. L. Tian, S. A. Hires, T. Mao, D. Huber, M. E. Chiappe, S. H. Chalasani, L. Petreanu, J. Akerboom, S. A. McKinney, E. R. Schreiter, C. I. Bargmann, V. Jayaraman, K. Svoboda, and L. L. Looger, "Imaging neural activity in worms, flies and mice with improved GCaMP calcium indicators," Nat. Methods **6**(12), 875–881 (2009).
6. W. Göbel, B. M. Kampa, and F. Helmchen, "Imaging cellular network dynamics in three dimensions using fast 3D laser scanning," Nat. Methods **4**(1), 73–79 (2007).
7. B. F. Grewe, F. F. Voigt, M. van 't Hoff, and F. Helmchen, "Fast two-layer two-photon imaging of neuronal cell populations using an electrically tunable lens," Biomed. Opt. Express **2**(7), 2035–2046 (2011).
8. G. Duemani Reddy, K. Kelleher, R. Fink, and P. Saggau, "Three-dimensional random access multiphoton microscopy for functional imaging of neuronal activity," Nat. Neurosci. **11**(6), 713–720 (2008).
9. B. F. Grewe, D. Langer, H. Kasper, B. M. Kampa, and F. Helmchen, "High-speed in vivo calcium imaging reveals neuronal network activity with near-millisecond precision," Nat. Methods **7**(5), 399–405 (2010).
10. G. Katona, G. Szalay, P. Maák, A. Kaszás, M. Veress, D. Hillier, B. Chiovini, E. S. Vizi, B. Roska, and B. Rózsa, "Fast two-photon in vivo imaging with three-dimensional random-access scanning in large tissue volumes," Nat. Methods **9**(2), 201–208 (2012).
11. L. Kong, J. Tang, J. P. Little, Y. Yu, T. Lämmermann, C. P. Lin, R. N. Germain, and M. Cui, "Continuous volumetric imaging via an optical phase-locked ultrasound lens," Nat. Methods **12**(8), 759–762 (2015).

12. W. Amir, R. Carriles, E. E. Hoover, T. A. Planchon, C. G. Durfee, and J. A. Squier, "Simultaneous imaging of multiple focal planes using a two-photon scanning microscope," Opt. Lett. **32**(12), 1731–1733 (2007).
13. E. J. Botcherby, R. Juškaitis, M. J. Booth, and T. Wilson, "An optical technique for remote focusing in microscopy," Opt. Commun. **281**(4), 880–887 (2008).
14. E. J. Botcherby, R. Juskaitis, M. J. Booth, and T. Wilson, "Aberration-free optical refocusing in high numerical aperture microscopy," Opt. Lett. **32**(14), 2007–2009 (2007).
15. E. J. Botcherby, C. W. Smith, M. M. Kohl, D. Débarre, M. J. Booth, R. Juškaitis, O. Paulsen, and T. Wilson, "Aberration-free three-dimensional multiphoton imaging of neuronal activity at kHz rates," Proc. Natl. Acad. Sci. U.S.A. **109**(8), 2919–2924 (2012).
16. M. Oheim, E. Beaurepaire, E. Chaigneau, J. Mertz, and S. Charpak, "Two-photon microscopy in brain tissue: parameters influencing the imaging depth," J. Neurosci. Methods **111**(1), 29–37 (2001).
17. A. Singh, J. D. McMullen, E. A. Doris, and W. R. Zipfel, "Comparison of objective lenses for multiphoton microscopy in turbid samples," Biomed. Opt. Express **6**(8), 3113–3127 (2015).
18. J. P. Zinter and M. J. Levene, "Maximizing fluorescence collection efficiency in multiphoton microscopy," Opt. Express **19**(16), 15348–15362 (2011).
19. J. Colon and H. Lim, "Shaping field for 3D laser scanning microscopy," Opt. Lett. **40**(14), 3300–3303 (2015).
20. E. H. Stelzer, "The intermediate optical system of laser-scanning confocal microscopes," in *Handbook of Biological Confocal Microscopy* (Springer, 2006), pp. 207–220.
21. P. Rupprecht, "ABCD optics for beam propagation for remote z-scanning," GitHub (2016). https://github.com/PTRRupprecht/remote-z-scanning-ABCD-optics
22. T. A. Pologruto, B. L. Sabatini, and K. Svoboda, "ScanImage: flexible software for operating laser scanning microscopes," Biomed. Eng. Online **2**(1), 13 (2003).
23. P. Zhu, O. Fajardo, J. Shum, Y. P. Zhang Schärer, and R. W. Friedrich, "High-resolution optical control of spatiotemporal neuronal activity patterns in zebrafish using a digital micromirror device," Nat. Protoc. **7**(7), 1410–1425 (2012).
24. T.-W. Chen, T. J. Wardill, Y. Sun, S. R. Pulver, S. L. Renninger, A. Baohan, E. R. Schreiter, R. A. Kerr, M. B. Orger, V. Jayaraman, L. L. Looger, K. Svoboda, and D. S. Kim, "Ultrasensitive fluorescent proteins for imaging neuronal activity," Nature **499**(7458), 295–300 (2013).
25. A. Suli, A. D. Guler, D. W. Raible, and D. Kimelman, "A targeted gene expression system using the tryptophan repressor in zebrafish shows no silencing in subsequent generations," Development **141**(5), 1167–1174 (2014).
26. R. Tabor, E. Yaksi, J.-M. Weislogel, and R. W. Friedrich, "Processing of odor mixtures in the zebrafish olfactory bulb," J. Neurosci. **24**(29), 6611–6620 (2004).
27. R. W. Friedrich, "Neuronal computations in the olfactory system of zebrafish," Annu. Rev. Neurosci. **36**(1), 383–402 (2013).
28. F. Blumhagen, P. Zhu, J. Shum, Y.-P. Z. Schärer, E. Yaksi, K. Deisseroth, and R. W. Friedrich, "Neuronal filtering of multiplexed odour representations," Nature **479**(7374), 493–498 (2011).
29. S. Junek, T.-W. Chen, M. Alevra, and D. Schild, "Activity Correlation Imaging: Visualizing Function and Structure of Neuronal Populations," Biophys. J. **96**(9), 3801–3809 (2009).
30. F. Helmchen and W. Denk, "Deep tissue two-photon microscopy," Nat. Methods **2**(12), 932–940 (2005).
31. H. P. Paudel, J. Taranto, J. Mertz, and T. Bifano, "Axial range of conjugate adaptive optics in two-photon microscopy," Opt. Express **23**(16), 20849–20857 (2015).
32. H. Dana and S. Shoham, "Remotely scanned multiphoton temporal focusing by axial grism scanning," Opt. Lett. **37**(14), 2913–2915 (2012).
33. J. N. Stirman, I. T. Smith, M. W. Kudenov, and S. L. Smith, "Wide field-of-view, twin-region two-photon imaging across extended cortical networks," bioRxiv **10**, 011320 (2014).
34. R. Prevedel, Y.-G. Yoon, M. Hoffmann, N. Pak, G. Wetzstein, S. Kato, T. Schrödel, R. Raskar, M. Zimmer, E. S. Boyden, and A. Vaziri, "Simultaneous whole-animal 3D imaging of neuronal activity using light-field microscopy," Nat. Methods **11**(7), 727–730 (2014).
35. M. B. Ahrens, M. B. Orger, D. N. Robson, J. M. Li, and P. J. Keller, "Whole-brain functional imaging at cellular resolution using light-sheet microscopy," Nat. Methods **10**(5), 413–420 (2013).

1. Introduction

Fast 3D imaging of large volumes at micrometer resolution is of high interest in the life sciences. In neuroscience, multiphoton laser scanning microscopy [1] is widely used for imaging of fluorescent calcium indicators to measure the activity of many neurons simultaneously in the intact brain [2–5]. However, large-amplitude scanning in the z-direction remains a challenge due to trade-offs between technical constraints and optical performance.

The most widely used methods for z-scanning are based on physical movements of the objective by piezo elements [6]. This approach is, however, limited by the inertia of the objective, may cause vibrations, and may exert pressure onto the sample through the immersion medium, particularly when the z-scan range is large. Movements of elements near the specimen can be circumvented by pre-focusing the laser beam with an electro-tunable lens [7] but this approach usually reduces the effective numerical aperture (NA) and strongly modulates the field of view (FOV). Alternatively, the beam can be manipulated with acousto-

optical deflectors (AODs) [8–10], which allows for fast random-access scanning in 3D. However, AODs introduce aberrations and require elaborated techniques to compensate for optical and temporal dispersion. Acoustic gradient index lenses operating at a fixed kHz frequency induce aberrations and have disadvantages for conventional plane scanning [11, 12].

A promising strategy for z-scanning is to insert a movable z-scan mirror into a conjugate focal plane of the specimen plane [13, 14]. Axial movements of the remote z-scan mirror change the divergence of the excitation beam, resulting in axial movements of the focus (Fig. 1(a)). High scan speeds can be achieved because the inertia of the mirror is minimal. When the optical magnification between the z-scan mirror and the sample is unity, the system can be aberration-free [14]. This strategy has been used successfully in a 3D multiphoton LSM [15] but the system has not been widely adopted, possibly because the beam path is complex and substantially different from that of a standard LSM. Moreover, for deep multiphoton imaging in the brain and other scattering media it is advantageous to use objectives with large back apertures (⌀ ≥18 mm) to maximize photon collection and the FOV [16–18]. Such objectives require an expansion of the excitation beam by a high-magnification telescope after the lateral scanning unit, which complicates the implementation of unity magnification.

We explored strategies for 3D multiphoton microscopy with a remote z-scan mirror that do not maintain unity magnification. We reasoned that effects of aberrations may be minor because multiphoton microscopy does not rely on the formation of an image on the detector. Moreover, aberrations caused by non-unity magnification may be small compared to other aberrations of the system and to resolution limitations due to scattering. The deviation from unity magnification enabled simple designs that do not require the use of a second high NA-objective for remote scanning. However, these designs required fast and accurate displacements of the z-scan mirror over large distances (>>1 mm). We found that this problem can be solved using a voice coil motor, an inexpensive device that is commonly used in low-to-mid frequency loudspeakers but also in industrial applications. Key features of voice coil motors are high positioning repeatability and high accelerations at low friction. Using this approach, a large axial scan range and high scan speeds could be achieved with minor loss of resolution.

The opto-mechanics of our z-scanning units (ZSUs) was contained in external modules that can be added onto a standard 2D multiphoton LSM. A compact z-scanning unit consisting of a single lens achieved an axial range of approximately 150 μm with an axial PSF of 2.6 – 7 μm full width at half maximum (FWHM) using a high-NA objective (20x; NA 1.0) with a large back aperture (⌀ 18 mm). By extending the ZSU with a telescope, the z-scan range was increased to >300 μm at the same resolution. Effective volumetric flyback times were between 5 and 15 ms, depending on the desired axial scanning amplitude. Using a multiphoton LSM with 8 kHz resonant scanners, 9 planes with 256 lines each could be scanned at a volume rate of 6 Hz. Using this approach, we measured activity patterns across >1500 neurons in the adult zebrafish brain by multiphoton calcium imaging.

2. Design of remote z-scanning units

2.1 Concept and trade-offs

Remote z-scanning can be achieved by inserting a movable z-scan mirror into a conjugate focal plane of the specimen plane (Fig. 1(a)) [14, 15, 19]. To implement this strategy in a laser scanning microscope (LSM) the excitation beam is passed through a ZSU containing an optional telescope with magnification $M' = f_1'/f_2'$ and a z-scan lens with focal length f_z (Fig. 1(b), 1(d)). Passage of the beam through the ZSU with minimal loss is achieved using a polarizing beam splitter (PBS) and a quarter-wave plate (QWP). When the distance between each pair of lenses is equal to the sum of their focal lengths (telecentric or 4f configuration [20]) and the magnification is unity ($f_o/M = f_z/M'$, neglecting possible immersion media), the system is, in theory, aberration-free [14] and the axial position of the focus changes linearly with the axial position of the z-scan mirror. In the absence of a telescope in the ZSU

(configuration 1, Fig. 1(b)) the displacement of the focus d relative to the focal plane f_o of the objective L_o is given by

$$d = -2\frac{f_0^2 f_2^2}{f_1^2 f_z^2}D \tag{1}$$

where D is the displacement of the z-scan mirror position relative to the focal plane of the z-scan lens, L_z. We analyzed the optical path using a linear propagation of Gaussian beams scheme. The underlying analytical derivations for this relation and all other equations in this paper have been documented and implemented in Mathematica (Wolfram), as we show in Code 1 (Ref [21].). In the presence of a telescope (configuration 2, Fig. 1(d)), the relation d(D) becomes

$$d = -2\frac{f_0^2 f_2^2 f_1'^2}{f_1^2 f_z^2 f_2'^2}D \tag{2}$$

Note that the telescope increases the axial scan range by a factor $(f_1'/f_2')^2 = M'^2$.
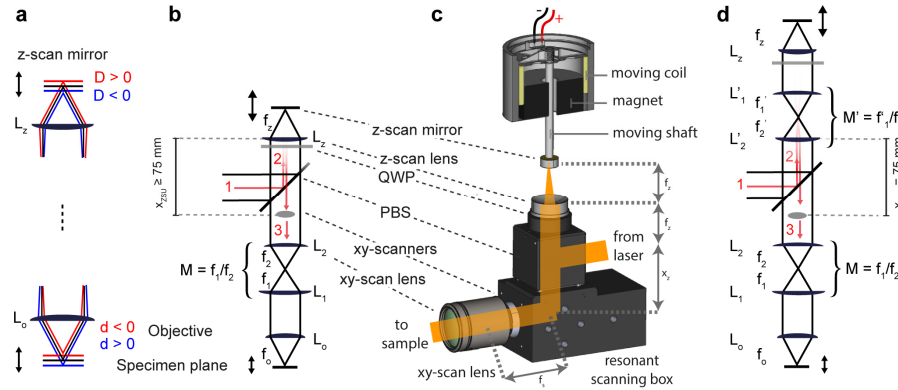

Fig. 1. Basic principle and design. (a) Basic principle. A remote z-scan mirror is inserted into a plane conjugate to the specimen plane. Moving the z-scan mirror away from this plane ($D \neq 0$) changes the divergence of the beam and displaces the focus ($d \neq 0$). (b) ZSU configuration 1 (single lens): the laser beam (1) is passed through the ZSU consisting of a single z-scan lens L_z with focal length f_z and the z-scan mirror (2) before reaching the xy scanners and the xy-scan lens L_2 (3). Directed passage of the beam is accomplished using a polarizing beam splitter (PBS) and a quarter-wave plate (QWP). The LSM consists of a scan lens (L_2) and a tube lens (L_1), which form a telescope with magnification $M = f_1/f_2$, and the objective (L_o). The minimum distance between the z-scan lens L_z and the xy-scanners is $x_{ZSU} = 75$ mm. (c) Experimental realization of configuration 1 (single-lens). The ZSU mounted onto the xy-scan unit is shown with correct relative scaling of the components. The discance x_{ZSU} between the z-scan lens and the xy-scanners is $x_{ZSU} = f_z + x_z = 75$ mm. This distance is required to insert the polarizing beam splitter, contained inside the cube, and the quarter-wave plate into the beam path. The voice coil motor is shown in a cross-sectional view, illustrating the working principle based on the coil inside a mostly homogeneous magnetic field. The z-scan mirror is attached to the coil by a rod and a scaffold. The Hall position sensor is glued to the top of the voice coil motor (not shown). (d) ZSU configuration 2 (with telescope). A second telescope with magnification $M' = f_1'/f_2'$ is inserted into the beam path of the ZSU. This permits to maintain telecentric distances between the intermediate optics system and to increase the focal shift d by a factor M'^2.

For previous implementations of this remote scanning strategy, a ZSU has been integrated into a LSM between the xy-scan mirrors and the xy-scan lens [15] or after the tube lens [19]. These implementations required relay beam paths that cannot be obtained by straightforward modifications of a standard LSM. We therefore considered integration of the ZSU in front of the xy-scan mirrors of a conventional 2D LSM (Fig. 1(b), 1(c)). Ideally, the ZSU should be contained in an external module to permit simple "upgrading" of existing 2D LSMs to 3D. As

our target application was multiphoton calcium imaging in the brain, our main requirements were (1) single-neuron resolution, (2) efficient filling of objectives with a large back aperture ($\varnothing \geq 18$ mm), (3) high axial scan speed, and (4) a large z-scan range (>100 µm; ideally >200 µm).

We assumed that a ZSU is added in front of a standard LSM with an objective (L_o; $f_o = 10$ mm), tube lens (L_1; $f_1 = 200$ mm), xy-scan lens (L_2; $f_2 = 50$ mm), and xy-scan mirrors approximately in the focal plane of L2 (Fig. 1(b), 1(d)). To accommodate the PBS and QWP, the distance x_{ZSU} between the xy-scan mirrors and the first lens of the ZSU was assumed to be ≥ 75 mm (Fig. 1(a)).

2.2 Configuration 1: single-lens ZSU

For the single-lens configuration, telecentricity requires that $x_{ZSU} = f_z$ and thus $f_z \geq 75$ mm. However, a z-scan range >200 µm in the sample would then require an unrealistically large displacement range of the z-scan mirror. We therefore considered a z-scan lens with $f_z = 30$ mm, resulting in deviations from the telecentric configuration with $x_z = 45$ mm. The axial displacement d of the beam focus in the sample as a function of the z-scan mirror displacement D is then given by

$$d = -2 \frac{f_0^2 f_2^2}{f_1^2 \left(f_z^2 - 2Dx_z \right)} D. \tag{3}$$

d(D) is nonlinear unless $x_z = 0$, i.e. $f_z = 75$ mm (Fig. 2(a)). Similar non-linear effects occur when an electro-tunable lens and a fixed mirror are used instead of a fixed lens and a movable mirror since telecentricity is not maintained (not shown).

The nonlinearity has two important consequences. First, the z-scan range in the sample is expanded for positive displacements D (towards L_z) and compressed for negative displacements D (away from L_z; Fig. 2(a)). Second, displacements of the z-scan mirror change the beam diameter R_{BA} at the back aperture of the objective:

$$R_{BA} = R \left(\frac{f_1}{f_2} - \frac{2Df_0 f_2}{f_1 f_z^2} - \frac{2Df_1 x_z}{f_2 f_z^2} \right). \tag{4}$$

R_{BA} decreases in the positive D-direction (towards L_z) which may result in underfilling of the objective's back aperture (Fig. 2(c)) and loss of resolution. In addition, displacements of the z-scan mirror can strongly modulate the FOV, as observed with an electro-tunable lens [7].

2.3 Configuration 2: ZSU with telescope

We next analyzed a ZSU with a telescope (Fig. 1d), which can maintain the telecentric configuration because f_2' can be chosen to be ≥ 75 mm. The relation d(D) is therefore linear (Fig. 2(b)) and the axial scan range increases quadratically with the magnification of the telescope $M' = f_1'/f_2'$ (Eq. (2)). In addition, we obtain

$$R_{BA} = R \left(\frac{f_1}{f_2} - \frac{2Df_1'^2 f_0 f_2}{f_1 f_2'^2 f_z^2} \right). \tag{5}$$

Since the second term is very small, R_{BA} is almost independent of the z-mirror displacement D and, thus, determined almost exclusively by the scan and tube lenses in the LSM (f_1/f_2). Filling of the objective's back aperture can therefore be maintained (Fig. 2(c)). For practical reasons we chose $f_1' = 150$, $f_2' = 75$ mm ($M' = 2$) and $f_z = 30$ mm. A scan amplitude of 10 mm thus translates into an axial scan range of approximately 550 µm (Fig. 2(b)). Ray tracing showed that the beam diameter in the relay lenses can reach 40 mm for the extreme values of the z-scan range (Fig. 2(c)). We therefore used 2-inch lenses for L'_1 and L'_2 and a 1-inch z-scan lens L_z.

Remote focusing using a telecentric configuration does not affect the FOV under the idealized assumption that the x- and y-scan mirrors are both positioned in the focal points of the relay lens L'_2 and the xy-scan lens L_2. In theory, such a configuration can be achieved with relay optics between the mirrors. In most LSMs, however, the mirrors are displaced from the focal points of L'_2 and L_2 by a distance w. We used the linear ABCD scheme to calculate the expected effects on the FOV based on the deflection angle β at the xy-scanners. The size of the FOV is given by

$$FOV \approx -\frac{f_0 f_2}{f_1} R \left(1 - \frac{2 f_1'^2}{f_2'^2 f_z^2} Dw\right)\beta \tag{6}$$

where R is the diameter of the incident beam and β is the x- or y-scan angle. The first term arises from xy scanning. The second term includes linear contributions of z-scanning (D) and the distance w.

Because w is different for the x- and y-scan mirrors, the modulation of the FOV is asymmetric. The asymmetry is given by the difference between the slopes of the relationship FOV(D) in x- and y-direction, which is determined by the distance Δw between the x- and y-scan mirrors. Assuming a realistic distance $\Delta w \approx 7$ mm and the lens parameters given above, Eq. (6) predicts that FOV modulation is modest (Fig. 2(d)). Because the expected practical consequences are minor, we did not introduce complex relay optics between the x- and y-scan mirrors.
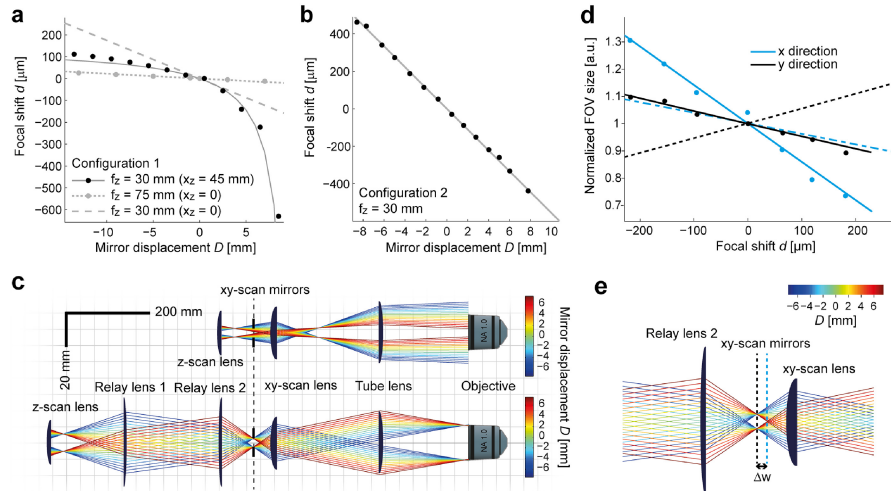

Fig. 2. Focal shift, back aperture filling and beam path. (a) Focal shift d as a function of mirror displacement D for configuration 1 (single lens). Dots show experimental measurements, lines show theoretical predictions (Eqs. (1), (2)). Black: z-scan lens with $f_z = 30$ mm; gray: z-scan lens with $f_z = 75$ mm. In both cases, $x_{ZSU} = 75$ mm. $x_z = x_{ZSU} - f_z$ gives the deviation from the telecentric arrangement. The dashed gray line shows theoretical prediction for $f_z = 30$ mm and $x_z = 0$, which was not realized experimentally. (b) Configuration 2 (telescope) with $f_z = 30$ mm ($x_z = 0$). The slope of the linear relationship d(D) is 56 µm/mm. (c) Schematic beam paths for single-lens (top) and telescope configuration (bottom). The diameter of the back aperture of the objective is approximately 18 mm. Rays indicate the outer shape of the beam; colors encode the z-scanning position. The focal length/free apertures of the xy-scan lens and the tube lens are 50 mm/30 mm and 200 mm/35 mm, respectively. The relay lenses have focal lengths/free apertures of 150 mm/50.8 mm and 75 mm/50.8 mm for the telescope configuration. Note that filling of the back focal aperture of the objective changes substantially during scanning in configuration 1 (single lens) but not in configuration 2 (telescope). (d) Modulation of FOV size in x and y direction as a function of focal shift d for configuration 2. Dots indicate measurements; solid lines show fits of Eq. (6) with $\Delta w = 7$ mm. Dashed lines indicate the theoretical FOV changes for $\Delta w = 7$ mm when the x- and y-scan mirrors are equidistant from the focal points of L'_2 and L_2. (e) Illustration of the separation of x- and y-scan mirrors by $\Delta w = 7$ mm in the beam path. All theoretical calculations for beam propagation were implemented in Mathematica, as we show in Code 1 (Ref [21]).

2.4 Fast axial scanning using a voice coil motor

The ZSU configurations considered above require z-scan amplitudes on the order of 10 mm which is beyond the range of fast piezo elements. Typical step motors used for objective or stage positioning cannot achieve the desired speed because their settling times are usually >100 ms. We therefore explored voice coil motors for z-scanning, which can produce fast and repeatable movements in the centimeter range and short settling times.

3. Experimental setup and performance evaluation

3.1 LSM, ZSU and voice coil motor

For all parts in the described setup, only off-the-shelf components were used in order to facilitate adaptation of our design. We customized a multiphoton LSM (MOM; Sutter Instruments) with a 200 mm tube lens, a 50 mm scan lens and a 20x objective (NA 1.0, f_o = 10 mm, Zeiss). The standard galvo xy-scanners were replaced by a galvo scanning/resonant scanning mirror pair (6215H and CRS 8 kHz, Cambridge Technology). The x-scan mirror was oval with a circular aperture of 5 mm and slightly smaller than the y-scan mirror. As a consequence, the maximum possible diameter of a non-divergent beam in the back focal plane of the objective was approximately 20 mm. xy-scanners were installed in a sound-attenuating scan head (Thorlabs, MPM-SCAN4) that was fixed to the central rail of the MOM system by a clamp (Thorlabs). Data were acquired using a high speed board with up to four input channels (Alazartech, ATS9440). Acquisition was triggered by the 80 MHz sync signal of the pulsed laser (Mai Tai, Newport Spectra-Physics) to allow for time-locked sampling relative to the fluorescence emission. The acquired raw data (4096 data points per line) were binned to the desired lateral resolution using a multithreaded routine written in C and streamed to a solid-state disk (SSD). All other parts of the microscope control software were programmed in MATLAB, loosely based on an existing freely available software (Scanimage 4.2 [22]).

A polarizing beam splitter (PBS) and a λ/4-wave plate (QWP) were used to direct the beam through the ZSU [15]. The PBS was contained in a cube that was mounted directly onto the case of the xy scan unit (Fig. 1(c)). The PBS inside the cube could be replaced with a mirror to bypass the ZSU if desired. The cube accepted a standard adapter to a 2" cage system that contained the telescope for configuration 2 (Thorlabs). The scan mirror (protected gold mirror, ø 12.7 mm, Thorlabs) was glued to an M6 nut, which in turn was fixed to the shaft of a voice coil motor (VM6548, GeePlus, Fig. 1(c)).
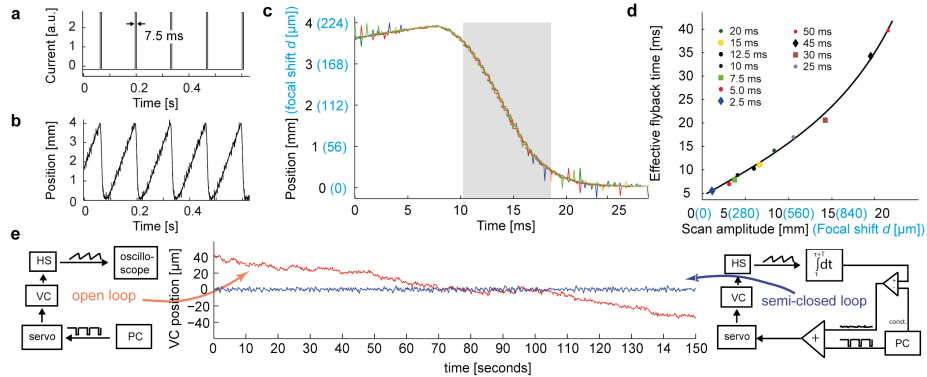
Fig. 3. Dynamics of the voice coil scanning system. (a) Step current pulses for sawtooth scanning. (b) Displacement of the voice coil motor measured with the position sensor. Small deflections are measurement noise, not positional noise. (c) Overlay of voice coil trajectories (different colors) during four successive flyback periods. Blue values on the y-axis show the corresponding focal shifts for configuration 2. Grey shading indicates the time when no data are acquired (effective flyback time). Steps in the curves are due to digitization. (d) Effective flyback time as a function of scan amplitude (black) and the corresponding focal shift for configuration 2 (blue). Black line is a spline fit. (e) Stabilization of the voice coil (VC) movement. In open loop the position of the VC is not controlled directly, leading to slow positional drift (red). In the semi-closed loop circuit, the positional signal of the hall sensor (HS) is integrated over one z-scan cycle and compared to the setpoint. An error signal proportional to the difference is added to the z-scanning command signal, preventing positional drift (blue).

The voice coil motor type (VM6548, GeePlus) was chosen because it provides high accelerations and long strokes (up to 20 mm). Voice coil motors with less stroke length but lower coil mass and considerably faster dynamics are available but have not been tested here since the tested motor was already sufficiently fast. We compared two different servo drivers for the voice coil motor (DA4709, Electrocraft; Junus JSP-090-10, Copley Controls) and found that the DA4709 model provided better control and stability for our implementation. For positional feedback, we glued the pole of a lightweight hall sensor (LHK hall sensor, Megatron) to the back of the voice coil motor.

3.2 Speed, precision and repeatability of the voice coil motor movements

To achieve spatially and temporally homogeneous volume sampling we used sawtooth-like z-scanning patterns. Within each z-scan period, multiple xy-planes are acquired during the slow movement of the z-scan mirror but no useful data is acquired during the fast return ("flyback"), resulting in a stack of images that are slightly tilted relative to the xy plane. To minimize the dead time during flyback, speed and acceleration of the z-scan mirror need to be sufficiently high. Assuming a desired volume scan rate ≥5 Hz, flyback times are desired to be <100 ms.

We tested whether z-scan mirror displacements with sufficient speed, amplitude, accuracy and repeatability can be produced by the voice coil motor. In order to determine the minimum possible flyback times we applied current inputs to generate sawtooth-like displacements and measured the trajectory of the coil. The amplitude of the current pulse was kept at maximum while the duration was varied between 2.5 ms and 50 ms. Because the position changes smoothly around the turning points, useful image data can be acquired not only during the slow phase but also during initial and final portions of the flyback period. We therefore operationally defined the effective flyback time as the time between 10% and 90% of the flyback amplitude. As expected, the effective flyback time increased almost linearly with the flyback amplitude. Nevertheless, the effective flyback time was short even when scan amplitudes were large. At a z-scan amplitude of 10 mm, the effective flyback time was approximately 15 ms (Fig. 3(d)).

We observed that the position of the voice coil can exhibit a slow drift in the absence of a position-dependent feedback. In order to stabilize the position on long time scales we therefore installed a computer-based slow control loop that read in the analog position output of the hall sensor, averaged the signal over one z-scan cycle, and compared it to the desired position. The difference was then proportionally fed on top of the fast z-scan signal using a simple differential amplifier (Fig. 3(e)). Closing the loop on this slow time-scale allowed for reliable positioning over very long timescales. The same circuit was used to ensure that successive scans started from the same z-position.

3.3 Z-scanning and optical performance

Using a ZSU with configuration 2 (telescope; $f_1' = 150$ mm, $f_2' = 75$, $f_z = 30$ mm), the relation d(D) was linear with a focal shift of 56 μm per mm displacement of the z-scan mirror, as predicted by Eq. (2) (Fig. 2(b)). We also observed a modest change in FOV size that depended linearly on D, as predicted by Eq. (6). Hence, the remote focusing performance of ZSUs in both configurations was in good agreement with analytical predictions.

Basic optical performance was assessed by the point spread function (PSF). Calcium imaging of neuronal population activity in the brain usually requires fluorescence measurements inside neuronal somata with a diameter of 7 − 25 μm. We therefore considered a PSF acceptable when the FWHM is ≤7 μm, although even lower values are preferred when activity is dense. Without a ZSU, the PSF of the LSM had a lateral FWHM of approximately 0.4 μm and an axial FWHM of 2.5 − 3 μm, consistent with an optimized system with a similar objective [10].

With a ZSU in configuration 1, the PSF was not noticeably different when the z-scan mirror was in the zero-position (D = 0; lateral and axial FWHM approximately 0.4 μm and 2.6 μm, respectively; Fig. 4(a), 4(b)). Displacements of the z-scan mirror broadened the PSF (Fig. 4(a), 4(b)). This effect was more pronounced in negative direction (D < 0), presumably because the objective became progressively more underfilled (Fig. 2(c)). Hence, displacements in negative direction can expand the z-scan range due to the nonlinear relationship d(D) but also compromise resolution when filling of the objective back aperture cannot be maintained. The axial FWHM of the PSF remained ≤7 μm within a z-scan range of approximately Δz = 150 μm (Fig. 4(a)). This range required a displacement of the z-scan mirror by ca. 18 mm, resulting in an effective flyback time of 30 ms.

With a ZSU in configuration 2, the PSF was again not noticeably different from the control condition without ZSU when the z-scan mirror was in the zero-position (D = 0; lateral and axial FWHM approximately 0.4 μm and 2.6 μm, respectively; Fig. 4(c), 4(d)). Displacements of the z-scan mirror broadened the PSF but this effect was less pronounced than in configuration 1 (Fig. 4(c), 4(d)). A PSF with an axial FWHM between 2.6 and 7 μm could be maintained throughout a z-scan range Δz of 370 μm (Fig. 4(c)). As a consequence of the 2x magnification by the telescope, this z-scan range required a displacement D of the z-scan mirror by only ca. 8 mm, resulting in an effective flyback time of ca. 12 ms (Fig. 3(d)).
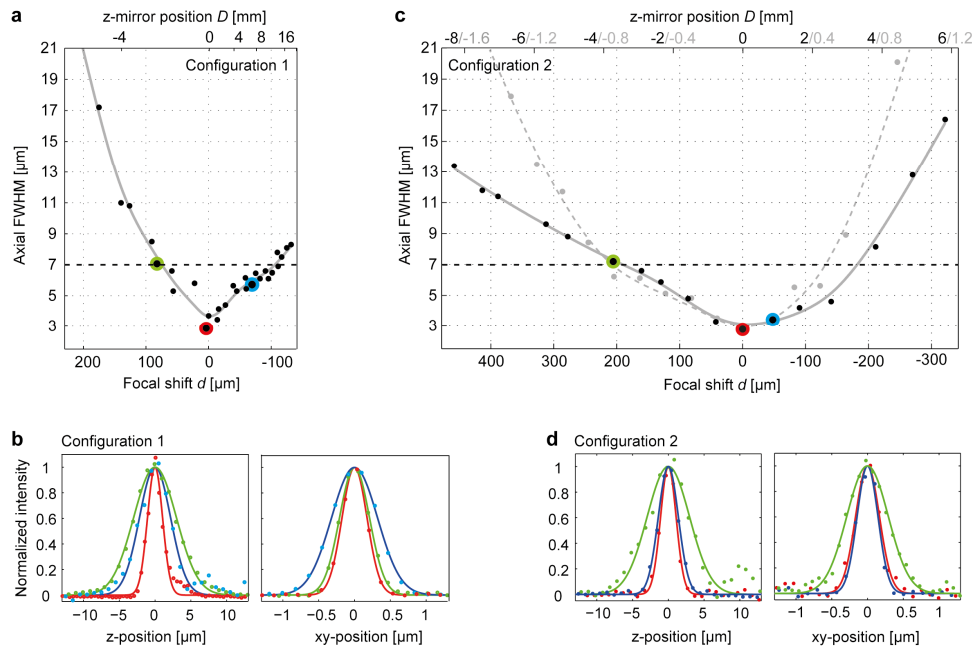
Fig. 4. Dependence of PSF on focal shift d. (a) Axial extent (FWHM) of the PSF as a function of focal shift d in configuration 1 (single lens). Corresponding z-scan mirror displacements D are shown on top. Black dots show measurements; grey line is a spline fit. Dashed line shows FWHM considered acceptable for multiphoton imaging of neuronal population activity (7 μm). (b) Examples of axial (left) and lateral (right) PSFs obtained in configuration 1 for different focal shifts d. Data are from the measurements marked by corresponding colors in (a). Individual data points show measurements; lines show Gaussian fits. (c) Black dots and continuous grey line: axial FWHM of the PSF as a function of focal shift d in configuration 2 (telescope; f_z = 30 mm). Gray dots and dashed line: same for f_z = 10 mm (20x objective as z-scan lens). (d) Examples of PSFs for configuration 2 (f_z = 30 mm). Data are from the measurements marked by corresponding colors in (c). For both configurations, the FWHM at d = 0 (red curves) was ca. 2.6 μm axially and 0.4 μm laterally.

Displacements of the z-scan mirror ($D \neq 0$) may broaden the PSF primarily because the deviation from unity magnification between the z-scanning mirror and the specimen plane introduces aberrations [14]. Alternatively, broadening of the PSF may be caused primarily by other factors, e.g. clipping of the beam at apertures such as the xy-scan mirrors, imperfect corrections of lenses, or effects of planar components such as the dichroic on strongly divergent beams. To examine whether deviations from non-unity magnification play a major role we replaced the 30 mm z-scan lens by a 20x objective identical to the objective of the LSM. The magnification from the z-scan mirror to the sample was therefore increased from ca. 0.17 to 0.5 while most of the beam path remained unchanged (Fig. 2(c)). Consistent with theoretical predictions Eq. (2), axial focus shifts d were more sensitive to displacements of the z-scan mirror D but the relationship remained linear (not shown). However, no obvious improvement of the PSF was observed compared to the configuration using a 30 mm z-scan lens (Fig. 4(c); dashed curve). We therefore hypothesize that the resolution was limited mainly by imperfections of optical components and/or by beam clipping at apertures, rather than by aberrations due to non-unity magnification.

4. Multiphoton calcium imaging in the adult zebrafish brain

The performance of ZSUs in practical applications was tested by 3D multiphoton calcium imaging of odor-evoked activity patterns in an ex-vivo preparation of the adult zebrafish brain [23]. Calcium signals were measured in stable transgenic lines expressing the genetically encoded fluorescent calcium sensor GCaMP6f [24] under the control of a fragment of the

neurod promotor (*Tg(NeuroD:GcaMP6F)$_{icm05}$*). To generate this line, the coding sequence of GCaMP6f was amplified by PCR from plasmid pGP-CMV-GCaMP6F (Addgene) and used to generate pME-GCaMP6F in a BP recombination reaction (Gateway system; Invitrogen). Subsequently, p5E-NeuroD [25], pME-GCaMP6F, p3E-poly(A), and pDest-pA2 were recombined in a 3-fragment LR reaction to generate NeuroD:GCaMP6f. This construct was injected into zebrafish embryos at the 1-cell stage in the following mixture: 35 ng/µL Tol2 transposase mRNA, 25 ng/µL NeuroD:GCaMP6F, 0.1 M KCl, 0.2% phenol red. F_0 larvae were screened for fluorescence, raised, and the transgenic insertion *Tg(NeuroD:GcaMP6F)$_{icm05}$* was identified in F_1 larvae. Imaging was performed in the olfactory bulb (OB) or in the posterior zone of the dorsal telencephalon (Dp), the teleost homolog of olfactory cortex. These brain areas contain small neurons (usually ≤10 µm) and have strongly curved surfaces.

Odors were applied to the nose using a custom-built odor delivery system. Figure 5 shows results obtained from the OB using a ZSU with configuration 1 (single-lens; f_z = 30 mm). Four planes with 512 x 512 pixels each were sampled at a volume rate of 7.5 Hz (Fig. 5(a)). Spacing of the planes was not even because d(D) was nonlinear. The centers of the first and last planes were separated by Δz_{center} = 75 µm. Because the planes were slightly tilted relative to the optical axis, the z-scan range between the extreme points was larger (Δz_{full} = 105 µm). Individual neurons could be clearly resolved in all planes. Expression of GCaMP6f was observed in subsets of neurons including mitral cells, the projection neurons of the OB, and interneurons. Characteristic neuropil regions of the OB, the olfactory glomeruli, were identified based on the high density of neuronal processes.

Most previous studies analyzed responses of neurons in the zebrafish OB to short odor presentations (<3 s) [26, 27]. Here we analyzed responses to longer stimuli, which are likely to be physiologically relevant [27, 28]. Two odors (25 µM alanine [Ala] and food extract) were applied for 40 s each while data were acquired continuously for 200 s (see Visualization 1). During each stimulus application, changes in fluorescence intensity relative to the baseline before odor application (ΔF/F) were calculated for each pixel. In these activity maps, individual somata and neuronal processes could be clearly resolved (Fig. 5(b), 5(c)).
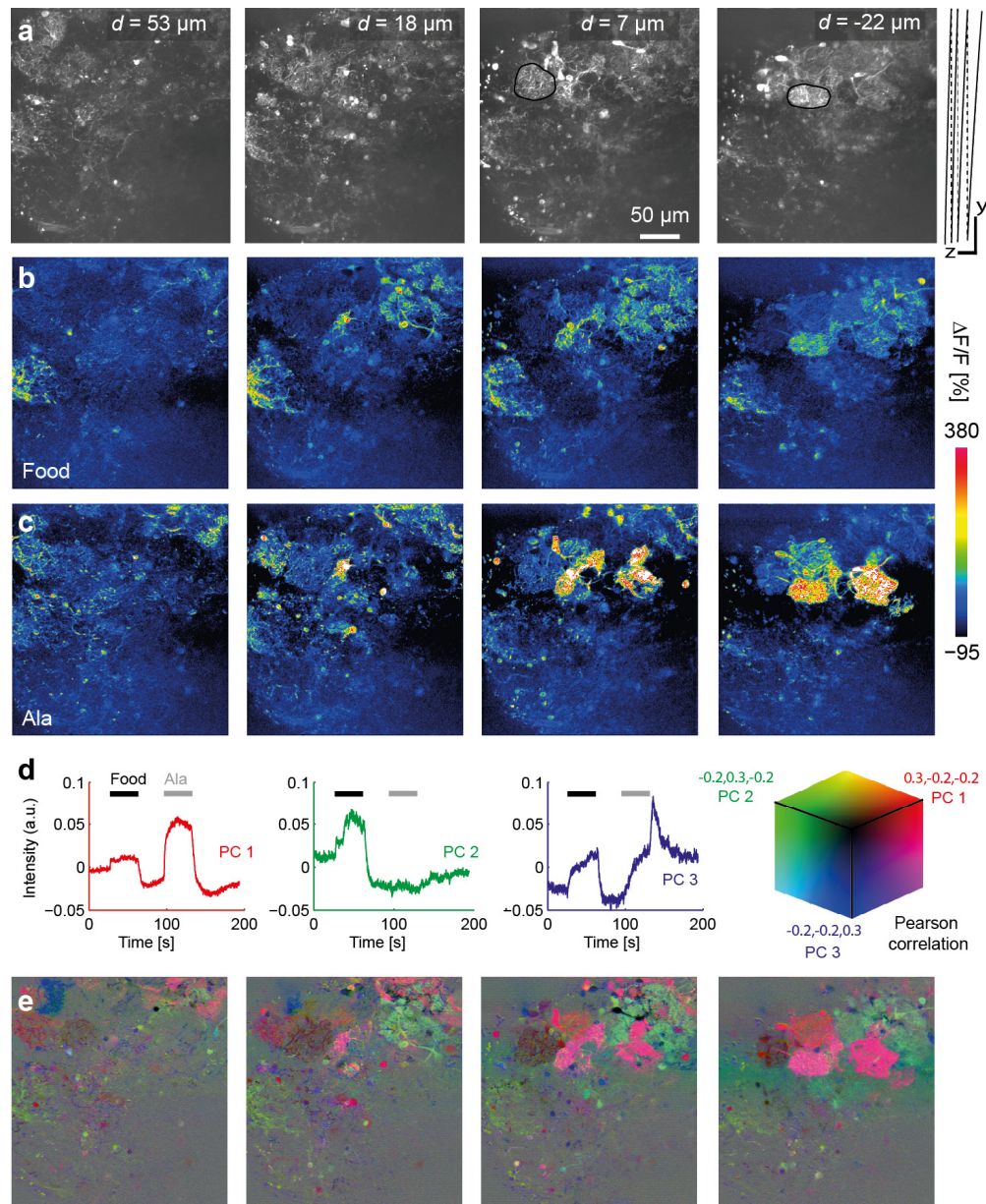
Fig. 5. Calcium imaging in the olfactory bulb using configuration 1. (a) Calcium indicator fluorescence (512 x 512 pixels) in four optical sections through the OB of an adult Tg(NeuroD:GcaMP6F)$_{icm05}$ fish (see Visualization 1). Values of d show the displacement of the center of each image from the reference plane (no mirror displacement; D = 0 and d = 0). Raw fluorescence images were averaged over the full 200 s. Two glomerular structures are outlined in black. Right: scan trajectory in yz; both scalebars are 50 µm. (b,c) Relative change in fluorescence intensity during application of each odor (40 s). (d) Time courses of first three principal components (PC 1-3) (e) Correlation maps showing the correlation coefficient between the time course of each pixel and each PC. For each optical section, the correlation maps for each PC are combined into a single RGB image (see color cube).

In order to analyze the dynamics of odor responses we defined regions of interest (ROIs) corresponding to 182 somata and 33 glomeruli and determined the time course of fluorescence changes (ΔF/F) in each ROI over the full 200 s. We then extracted the first three principal components (PCs) from the time series of all ROIs (Fig. 5(d)). Each PC thus

represents a fundamental component of the dynamics of the population activity. We then computed the correlation coefficient between the time course of the fluorescence in each pixel and each PC to obtain three correlation maps per image plane, one for each PC. The three correlation maps were then combined into single RGB images (Fig. 5(e)). The final RGB image thus represents the contribution of each PC to the dynamics of the fluorescence signal in each pixel. This analysis showed that PC1, which captured the time course of stimulus presentation, contributed strongly to responses of glomerular neuropil regions. The temporally more complex PCs 2 and 3, in contrast, were correlated mainly with responses of dispersed subsets of somata. Sharp morphological representations of individual neurons and even their processes could be resolved in correlation maps of all four image planes. Similar results were obtained in additional experiments in the OB and Dp (11 experiments in 3 fish). Together, these results demonstrate that volumetric multiphoton calcium imaging with high resolution and signal-to-noise ratio can be achieved using a ZSU with configuration 1 throughout a z-scan range of at least 100 μm.

Figure 6 shows results obtained from anterior Dp using a ZSU with configuration 2 (telescope). Nine sagittal planes, each with 512 x 256 pixels, were imaged at a volume scan rate of 6 Hz. The z-scan range was $\Delta z_{center} = 238$ μm and $\Delta z_{full} = 267$ μm (Fig. 6(c), 6(d)), covering the full depth of anterior Dp. Homogeneous expression of GCaMP6f was observed throughout anterior Dp. Assuming a scattering length of $l_s = 200$ μm [30], it is likely that scattering of the excitation light compromised image resolution in the deep planes. Consistent with this assumption, the apparent sharpness of images decreased slightly with depth. No obvious decrease in sharpness was observed in the most superficial planes even though the displacement of the z-scan mirror D was larger than for the deep planes. These observations indicate that scattering of the excitation light had a larger influence on resolution than remote focusing. Overall, however, resolution remained high throughout the full z-scan range because individual somata with diameters down to 5 μm could be clearly resolved in all planes.

Two odors (25 μM Ala and food extract) were applied twice for 40 s each during continuous data acquisition for 400 s (see Visualization 2). ROIs corresponding to 1507 somata (Fig. 6(b)) were outlined manually and classified into four clusters by the k-means algorithm based on their fluorescence time courses. The first and second clusters showed different excitatory on- and off-responses to the two odors (Fig. 6(e), red and blue) while the third cluster (green) was inhibited by both odors. Each ROI was RGB-coded as in Fig. 5(e) based on the Pearson correlation coefficient between its fluorescence time course and the mean time courses of the first three clusters. This analysis allowed us to map the modes of the population response that are represented by the first three clusters to somata throughout anterior Dp (Fig. 6(b)). While a band of neurons near the caudal end of anterior Dp was primarily associated with cluster 2, no obvious topographic organization was observed in other regions. Moreover, responses of individual ROIs were diverse and often not closely associated with a single cluster (Fig. 6(f)). High spontaneous activity was observed at intermediate depths but odor responses occurred throughout all planes. Similar results were obtained in 64 experiments in 8 fish. These results demonstrate that ZSUs with configuration 2 allow for efficient multiphoton imaging of neuronal activity throughout large volumes.

5. Discussion

We developed simple and versatile methods for fast 3D multiphoton laser scanning microscopy by remote focusing with a movable z-scan mirror. Imaging the z-scan mirror into the specimen plane with unity magnification can prevent aberrations [14] but imposes technical constraints. We released the constraint of unity magnification and found that the resulting aberrations had only minor effects on resolution throughout a large z-range. This enabled the development of self-contained ZSUs that can be added onto standard LSMs. Using these ZSUs, the activity of large numbers of neurons was measured in the intact zebrafish brain with high speed and resolution.
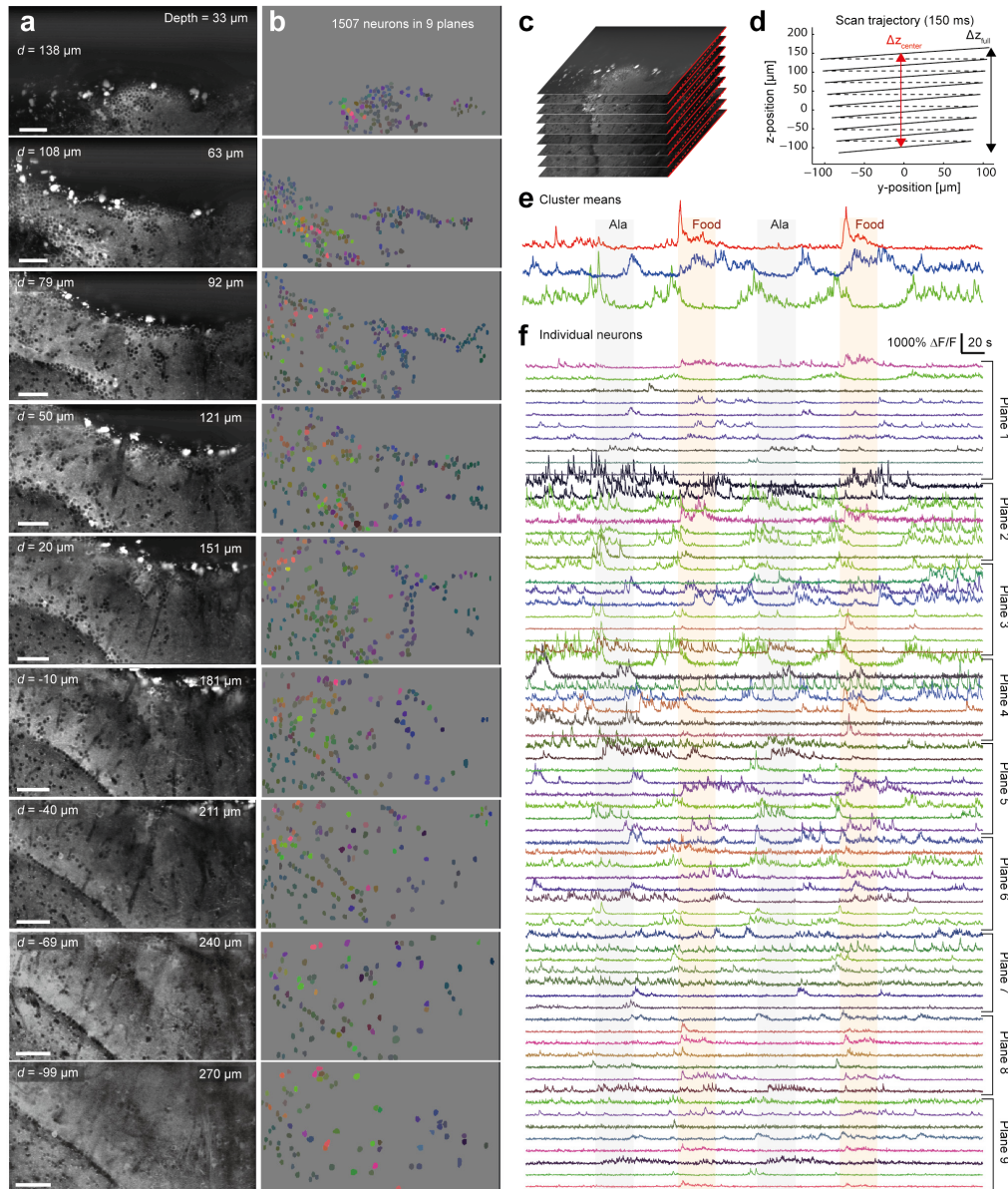
Fig. 6. Calcium imaging in Dp using configuration 2. (a) Fluorescence in each plane, averaged over the full duration of 400 s (see Visualization 2). d indicates the focal shift d(D), 'depth' the axial distance of the plane from the brain surface. All scale bars are 50 μm. (b) ROIs depicting clearly identified somata of 1507 neurons. Colors encode the correlation between the fluorescence time courses of each ROI and the first three clusters (e) in RGB (see Fig. 5(e)). (c) Schematic depiction of scanned planes. (d) Scan trajectory in yz. Planes were tilted (angle, 9.5°) and lower planes were slightly smaller due to FOV compression. Dashed lines indicate flybacks of the y-scanner. (e) Time courses of fluorescence signals averaged over ROIs of the first three activity clusters. Color corresponds to the RGB code in (b) and (f). Shading depicts periods of odor application. (f) Fluorescence time courses of subsets of ROIs from each plane. RGB color code shows correlation to the time course of each cluster (e).

The use of a voice coil motor permitted fast and precise displacements of the z-scan mirror over large distances to produce focal shifts >500 μm. The speed allowed for axial sawtooth scanning with effective flyback times of 5 – 15 ms, enabling highly efficient data collection. Using standard 8 kHz resonant scanners, 2D images with 256 or 512 lines can be

acquired at ca. 60 or 30 Hz, respectively. At a volume scan rate of 6 Hz it is therefore possible to acquire data from 9 image planes with 256 lines or 4.5 image planes with 512 lines. The high speed and accuracy of voice coil motors may also be exploited for fast long-range positioning of optical components in a broad range of other applications [19, 31, 32].

Effects of remote focusing on the PSF were modest and appeared to be dominated by imperfections of optical components rather than by aberrations due to non-unity magnification. Using a ZSU in configuration 2 (with telescope), broadening of the PSF was minimal within a commonly used z-scan range of 100 − 150 μm (50 − 75 μm in each direction; Fig. 4(c), 4(d)). A PSF with an axial FWHM ≤7 μm was maintained throughout a z-scan range of ~370 μm. Theoretically, broadening of the PSF may be further reduced by detailed simulations and optimizations of optical components in the ZSU. However, at high imaging depth, resolution is typically compromised by scattering of excitation light [30]. Further improvements of the PSF are therefore expected to produce only minor practical benefits unless other limiting effects are also compensated.

Compared to piezo-based movements of the objective [6], z-scanning with a remote mirror has the advantage that it is not limited by the inertia of the objective. This is particularly important when heavy objectives are used to image large FOVs [33]. Moreover, no pressure variations are transduced to the sample through the immersion medium. Unlike approaches using electro-tunable lenses or acoustic gradient index lenses [7, 11], purely mechanical z-scanning avoids imperfections of tunable components. 3D multiphoton microscopy of large volumes with optical performance similar to ours can be achieved using AODs but this approach requires complex equipment to compensate for undesired optical effects [10].

Our ZSUs have been developed primarily for multiphoton imaging of somatic calcium signals throughout large volumes in the intact brain. To maximize photon collection in strongly scattering tissue we accommodated large objectives in order to maintain a high effective NA. Homogeneous sampling throughout a volume was achieved using sawtooth-like scan patterns but other scan patterns including 3D line trajectories could also be generated. The limiting scan frequency of voice coil motors with large stroke is ~100 Hz. In principle, frequencies in the kHz range could be achieved using voice coil motors with smaller stroke when an objective is used as a z-scan lens. However, such high frequencies are of interest mainly for line scanning, which can also be performed using other methods [9, 10, 15]. Other approaches for fast homogeneous sampling of large volumes are light sheet or light field microscopy [34, 35]. However, multiphoton scanning microscopy is expected to provide higher resolution in a regime of strong scattering. Moreover, unlike light sheet microscopy, it does not require optical access from different directions, which is often difficult to achieve in vivo.

Besides optical performance and speed, important goals governing the design of our ZSUs were simplicity, versatility and cost-effectiveness. All components can be obtained off-the-shelf at a total cost of <2,500 EUR. Importantly, ZSUs can be added onto standard LSMs without modifying the LSM itself, allowing for upgrades of existing instruments. We explored two possible configurations. Configuration 1 includes a single lens and is very compact. Because it does not maintain telecentricity, optical performance depends strongly on the z-scan range and z-scanning is not linear. However, these effects are modest within a z-scan range up to approximately 150 μm. This design is therefore attractive for applications that require small z-scan ranges. Configuration 2 contains a telescope and is slightly more complex. Scanning behavior is linear, allowing for equal spacing of image planes, and optical performance is maintained over an extended z-scan range. This design is therefore useful for a wider range of applications including 3D scanning of large volumes.

Multiphoton calcium imaging of neuronal activity patterns in the intact brain is an important approach to analyze neuronal codes and information processing by neuronal circuits. ZSUs for remote focusing provide a simple solution to extend multiphoton calcium imaging to the third dimension without major compromises on optical performance or functionality. We measured odor-evoked calcium signals in the intact zebrafish brain in

multiple focal planes over long periods of time. The signal-to-noise ratio and resolution were comparable to those obtained by 2D scanning. Even small neurons and neuronal processes could be resolved throughout large volumes, confirming the efficiency of the approach in practical applications.

Simultaneous and dense measurements of odor responses from large numbers of neurons allowed us to analyze the dynamics of neuronal population responses in the OB and Dp, and to map fundamental components of the dynamics back onto individual neurons in 3D. In both brain areas, we observed complex population dynamics without a straightforward topographic organization. These results provide a starting point for more detailed analyses of neuronal population responses in the olfactory system. Moreover, they illustrate how 3D multiphoton calcium imaging can address fundamental questions in neurobiology that are difficult to address by other methods.

Acknowledgments